Proceedings of the ASME 2018
Conference on Smart Materials, Adaptive Structures and Intelligent Systems
SMASIS2018
September 10-12, 2018, San Antonio, TX, USA

SMASIS2018-8123

ANALYTICAL MODELING OF A MULTIFUNCTIONAL SEGMENTED LITHIUM ION BATTERY UNIMORPH ACTUATOR

Cody Gonzalez*
Department of Mechanical and Nuclear Engineering
The Pennsylvania State University
University Park, Pennsylvania 16802
Email: cag46@psu.edu

Jun Ma
Department of Mechanical and Nuclear Engineering
The Pennsylvania State University
University Park, Pennsylvania 16802
Email: jxm1153@psu.edu

Mary Frecker
Professor
Department of Mechanical and Nuclear Engineering
The Pennsylvania State University
University Park, Pennsylvania 16802
Email: mxf36@psu.edu

Christopher Rahn
Professor
Department of Mechanical and Nuclear Engineering
The Pennsylvania State University
University Park, Pennsylvania 16802
Email: cdrahn@psu.edu

ABSTRACT

Silicon anodes in lithium ion batteries have high theoretical capacity and large volumetric expansion. In this paper, both characteristics are used in a segmented unimorph actuator consisting of several Si composite anodes on a copper current collector. Each unimorph segment is self-actuating during discharge and the discharge power can be provided to external circuits. With no external forces and zero current draw, the unimorph segments will maintain their actuated shape. Stress-potential coupling allows for the unimorph actuator to be self-sensing because bending changes the anodes' potential. An analytical model is derived from a superposition of pure bending and extensional deformation forces and moments induced by the cycling of a Si anode. An approximately linear relationship between axial strain and state of charge of the anode drives the bending displacement of the unimorph. The segmented device consists of electrically insulated and individually controlled segments of the Si-coated copper foil to allow for variable curvature throughout the length of the beam. The model predicts the free deflection along the length of the beam and the blocked force. Tip deflection and blocked force are shown for a range of parameters including segment thicknesses, beam length, number of segments, and state of charge. The potential applications of this device include soft robots and dexterous 3D grippers.

*Address all correspondence to this author

1. INTRODUCTION

A unimorph actuator is composed of an active layer bonded to a passive layer. When the active layer is actuated the induced strain bends the composite beam. Lithium ion batteries (LIB) have an anode, separator for electrical insulation, and a cathode, all saturated in liquid electrolyte. Silicon (Si) anode material has strong potential for use in lithium ion batteries (LIB's) due to its high theoretical capacity [1]. Si also has large volumetric expansion, making it a potential actuator material. By coating a Si nanoparticle composite anode on a copper foil current collector to create a unimorph, the large volumetric expansion causes the unimorph to bend.

In this paper, a segmented LIB unimorph with Si anodes is introduced. The compliance of the segmented unimorph beam can be localized and tailored to allow for excellent range of motion and dexterity in applications such as a three-dimensional gripper. The 3D gripper would allow for the even distribution of force throughout each finger due to the self-sensing and self-powering nature of the actuator. A self-powered actuator does away with the need for external power cables or pneumatic actuation as is often the case with contemporary soft robots. Si has a stress-potential coupling effect, such that it experiences a change in voltage when external force is applied. This stress-potential coupling effect can be used to sense the amount of beam deflection. This effect can potentially allow for a self-sensing effect that may eliminate the need for external control as well. Better understanding of self-powered multi-segmented actuators can pave the way for advancement in the field of soft robotics. However, before the segmented actuator modeling is addressed, related work on lithium ion battery modeling is presented below.

Figure 1 shows a schematic of a typical Li-ion battery consisting of four components: cathode, anode, separator and electrolyte [2]. The cathode and anode consist of active material coated on current collectors. During charging, Li-ions diffuse out of the cathode, migrate through electrolyte and separator and insert the anode. This process causes cathode potential to increase and anode potential to decrease. In this way, a Li-ion battery converts electrical energy to chemical energy. The discharging is the reverse process that releases the energy and provides power to external load.

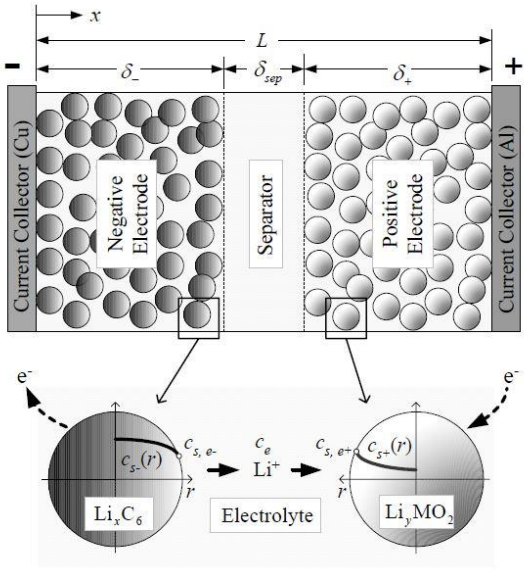

FIGURE 1. Composite electrode LIB configuration [2].

Various models have been developed to evaluate a battery's voltage, state of charge (SOC) and state of health (SOH) based on current input. Since a Li-ion battery is a nonlinear system consisting of mass and charge transport in solid and liquid phases, three-dimensional, full order modeling requires significant computational resources [3–5]. A widely used simplified model is the single particle model (SPM) [6,7]. In this model, it is assumed that electrode particles are connected in parallel and current is distributed uniformly. Therefore, each electrode can be represented with a spherical particle. The mass and charge transport process in the solid phase is simplified in 1D spherical coordinates. This model offers sufficient accuracy for most applications with reasonable computational cost [8]. With the Padé approximation, the SPM has become even faster, making it suitable for control purposes [2,9].

In related work on unimorph and bimorph segmented actuators, electroactive polymers [10,11], piezoelectric materials [12–19], and electromagnetic actuators [20] have been considered. These are often modeled for 2-D doubly-clamped cases [18], though 3-D piezoelectric actuation has been considered as well [14,15]. Among the models used for analysis of segmented beams, there are typically two modeling approaches, analytical [13,17] and finite element analysis (FEA) methods; combinations of both have also been considered [14–16]. Crawley *et al.* developed models for induced actuation strain in beam structures and analyzes piezoceramics in particular [12]. Our model seeks to fill the research gap in analytical modeling of segmented unimorph beams for electrochemical actuation.

It is worth noting that there are several approaches for large deflection analysis. The main methods for large deflection analysis of beams are elliptic integral solutions,

pseudo-rigid body model, analytical models based off the moments and forces experienced by the beam, fine element analysis, and chain algorithms. Howell notes that elliptic-integral solutions require complicated derivations and are only able to solve for relatively simple geometries and loadings. [21]. He goes on to state that the simplifying assumptions of linear material properties and inextensible members can be further limiting such that more flexible members require alternative methods of analysis. Common alternatives to elliptic integral solutions include finite element analysis and chain algorithms which use the same theories but different solution techniques. These methods can be computationally costly.

2. SEGMENTED ACTUATOR CONCEPT

The segmented unimorph actuator can be designed two ways. First, it can consist of a series of independently actuating and electrically isolated coating layer segments that are able to maintain different states of charge. This requires a complex wiring design since each segment is wired independently. Second, the segmented actuator can also be designed to generate non-uniform curvature by electrically connecting segments of varying thickness at a constant state of charge throughout the length of the beam. Figure 1 shows the uniform thickness configuration of the model of an active composite Si nanoparticle coating on a copper foil passive layer.

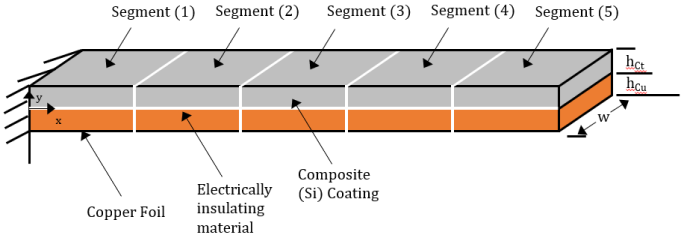

FIGURE 2. Segmented Unimorph Actuator

Activation of the composite Si coating layer is caused by charging the battery, such that increasing the state of charge increases the free deflection of the actuator. By controlling the state of charge in each electrically isolated segment, non-uniform curvature can be achieved. For an electrically connected segmented beam, the thicknesses of the active and passive layer can be tuned to allow for greater or lesser curvature in different segments of the beam to tailor the curvature at constant state of charge. This would require only one controller for a uniform state of charge throughout the length of the beam.

3. ANALYTICAL MODEL

The analytical model of the segmented unimorph actuator is derived based on beam bending theory accounting for large deflections and the induced axial strain in the coating layer caused by lithium insertion. This model is adapted in part from earlier work on modeling electroactive polymer actuators [10]. The stress in the unimorph at the interface T_1 is:

$$T_1 = E_{ct}(S_1 + S_1^*) \tag{1}$$

where E_{ct} is the elastic modulus of the active coating layer and S_1 is the transverse strain experienced in response to the coating layer axial strain upon lithium insertion, S_1^*. This actuation strain is assumed to be equal to the product of the normalized average lithium concentration $\hat{C}_{Li}$ and the linear strain rate β:

$$S_1^* = \beta \hat{C}_{Li} \tag{2}.$$

The linear strain rate is estimated through a single particle anode model to be 5%, and the normalized average lithium concentration is estimated to range between 0 and 0.9680 [22]. While the normalization would usually range from zero to one, the slight offset from maximum lithium concentration is due to the protocol used when charging lithium ion batteries to below the maximum state of charge (SOC) for prolonged life.

3.1 Pure Extensional Deformation

Upon activation, the coating layer causes an extensional force in the beam shown in equation (3). The extensional or axial force F_{ext} is:

$$F_{ext} = \int_t T_1 w dy = \int_{h_{Cu}-h}^{h_{Ct}+h_{Cu}-h} \left(E_{Ct}S_1 + E_{Ct}\beta \hat{C}_{Li}\right) w dy + \int_{-h}^{h_{Cu}-h} (E_{Cu}S_1) w dy \tag{3}$$

where the distance to the neutral axis h is equal to

$$h = \frac{E_{Ct}h_{Ct}h_{Cu} + E_{Cu}\frac{h_{Cu}^2}{2} + E_{Ct}\frac{h_{Ct}^2}{2}}{E_{Ct}h_{Ct} + E_{Cu}h_{Cu}}. \tag{4}$$

Here y is measured from the neutral axis, w is the width of the actuator, and E_{Ct} and E_{Cu} are the elastic moduli of the coating layer and copper foil, respectively. The thicknesses of the coating layer and copper layer are h_{Ct} and h_{Cu}, respectively. Solving the integral results in equation (5), where S_1 is assumed to be the extensional strain in the midplane:

$$F_{ext} = EA_e S_1 + E_{Ct}A_{Ct}\beta \hat{C}_{Li} \tag{5}$$

where the sum of the products of the respective elastic moduli and cross-sectional areas EA_e is:

$$EA_e = E_{Ct}A_{Ct} + E_{Cu}A_{Cu}. \tag{6}$$

Here A_{Ct} and A_{Cu} are the cross-sectional areas of the coating and copper foil layers, respectively, and are equivalent to the product of the width of the beam w and the respective thicknesses h_{Ct} and h_{Cu}.

The extensional force applied away from the midplane causes a bending moment M_{ext} which is shown in equation (7):

$$M_{ext} = \int_{h_{Cu}-h}^{h_{Ct}+h_{Cu}-h} \left(E_{Ct}S_1 + E_{Ct}\beta\hat{C}_{Li}\right)wydy + \int_{-h}^{h_{Cu}-h}(E_{Cu}S_1)wydy. \quad (7)$$

By solving the integrals in equation (7), the expression in equation (8) results as:

$$M_{ext} = \alpha S_1 + \frac{1}{2}E_{Ct}A_{Ct}(h_{ct} - 2h + 2h_{cu})\beta\hat{C}_{Li} \quad (8)$$

where the constant α is defined in equation (9).

$$\alpha = \frac{1}{2}[E_{Ct}A_{Ct}(h_{Ct} - 2h + 2h_{Cu}) - E_{Cu}A_{Cu}(2h - h_{Cu})]. \quad (9)$$

3.2 Pure Bending Deformation

Assuming linearly elastic behavior, a resultant force F_{bend} is caused by the bending curvature as derived in equation (10):

$$F_{bend} = \int_{h_{cu}-h}^{h_{ct}+h_{cu}-h}(E_{ct}\kappa y)wdy + \int_{-h}^{h_{cu}-h}(E_{Cu}\kappa y)wdy \quad (10)$$

where κ is the curvature. This bending force is due to the strain mismatch between the two layers. The actuation strain S_1^* is already accounted for in the extensional deformation terms and does not need to be accounted for in the bending terms. When solving, an expression for F_{bend} is found to be the product of the curvature κ and the constant α from equation (9):

$$F_{bend} = \kappa\alpha. \quad (11)$$

The bending moment M_{bend} due to the pure bending deformation is:

$$M_{bend} = \int_{h_{cu}-h}^{h_{ct}+h_{cu}-h}(E_{ct}\kappa y)wydy + \int_{-h}^{h_{cu}-h}(E_{Cu}\kappa y)wydy. \quad (12)$$

This simplifies to the product of the curvature κ and the equivalent bending stiffness EI_e of the beam (Equation 13) found using standard analysis of a composite beam found in equations (14a-c):

$$M_{bend} = kEI_e \quad (13)$$

$$EI_e = E_{Ct}I_{Ct} + E_{Cu}I_{Cu}. \quad (14a)$$

Here the area moment of inertia of the coating layer is:

$$I_{Ct} = \frac{1}{12}wh_{Ct}^3 + A_{Ct}\left(h_{Cu} + \frac{h_{Ct}}{2} - h\right)^2 \quad (14b)$$

and the area moment of inertia of the copper foil is:

$$I_{Cu} = \frac{1}{12}wh_{Cu}^3 + A_{Cu}\left(\frac{h_{Cu}}{2} - h\right)^2 \quad (14c)$$

3.3 *Superposition*

Superimposing the extensional and bending force and moment equations allows for the total force and moment to be calculated. Without any applied external forces, the sum of forces and moments are equal to zero, and we can combine equations (5) and (11) as well as (8) and (13) to solve for the extensional strain and curvature. The total force F_T and total moment M_T are:

$$F_T = F_{ext} + F_{bend} = 0 \quad (15a)$$
$$M_T = M_{ext} - M_{bend} = 0 \quad (15b)$$

such that solving the system of equations (15a) and (15b) allows for the determination of the curvature (16a):

$$\kappa = \frac{\alpha S_1 + \frac{1}{2}E_{Ct}A_{Ct}\beta\hat{C}_{Li}(h_{Ct} - 2h + 2h_{Cu})}{EI_e}. \quad (16a)$$

where the extensional strain S_1 is defined as:

$$S_1 = -\frac{E_{Ct}A_{Ct}\beta\hat{C}_{Li}[\frac{EI_e}{\alpha} + \frac{1}{2}(h_{Ct} - 2h + 2h_{Cu})]}{\frac{EI_e(EA_e)}{\alpha} + \alpha}. \quad (16b)$$

3.4 *Nodal Deflection*

As Si has a large volumetric expansion, it is important to account for large deflections in the analysis of the model. In the calculation of the deflection, it is assumed the curvature induced by the actuation strain of the Li insertion is due to an equivalent end moment, M_{eq}, on a passive beam. For a cantilever beam with an end-moment, the Bernoulli-Euler equation is given as:

$$\frac{M_{eq}}{EI_e} = \frac{d\theta}{ds} = \kappa \quad (17)$$

where θ is the beam angle or slope, s is the distance along the beam or arc length, EI_e is the equivalent bending stiffness of the beam, and $\frac{d\theta}{ds}$ is equivalent to the curvature

κ. The equivalent end moment M_{eq} due to the actuation strain caused by lithium insertion is found by substituting the curvature value found in (16a) into (17).

To obtain the deflection angle θ_0 (19) at the beam tip, we perform a separation of variables and integrate both sides as shown in equation (18) where $(x_2 - x_1) = l$ is the length of the beam:

$$\int_0^{\theta_0} d\theta = \int_{x_1}^{x_2} \frac{M_{eq}}{EI_e} ds \tag{18}$$

$$\theta_0 = \frac{M_{eq}(x_2 - x_1)}{EI_e} = \frac{M_{eq} l}{EI_e}. \tag{19}$$

It is worth noting that because the integration is with respect to s and not x, there is no small deflection assumption being made. We can apply the chain rule of differentiation to equation (17), perform a separation of variables, and then integrate both sides to find the vertical deflection δ_y and the horizontal deflection δ_x. An example of which is shown in equation (20):

$$\int_0^{\delta_y} dy = \frac{EI_e}{M_{eq}} \int_0^{\theta_0} \sin\theta \, d\theta. \tag{20}$$

By solving the integrals and finding δ_x in a similar way we can calculate both deflections as follows:

$$\delta_y = EI_e \frac{(1 - cos\theta_0)}{M_{eq}} = \frac{1}{\kappa}(1 - cos\kappa l) \tag{21}$$

$$\delta_x = l - EI_e \frac{sin\theta_0}{M_{eq}} = l - \frac{sin\kappa l}{\kappa}. \tag{22}$$

3.5 Calculation of nodal deflections for multiple segments

For a small number of segments along the length of the beam N, it is possible to calculate the deflected coordinates of the tip of each segment in the global coordinate system. A local coordinate system is created at the base of each segment which is rotated at $\theta_{locali} = \theta_0$ due to the previous segment's actuation where θ_0 is calculated in equation (19). The rotation angle θ_i for the ith segment in the global coordinate system is shown in equation (23).

$$\theta_i = \theta_{locali} + \theta_{i-1} \tag{23}$$

The x and y components of the tip deflection of each segment are calculated in the local coordinate system such that $\delta_{ylocali} = \delta_y$from equation (21) and $\delta_{xlocali} = \delta_x$ from equation (22). These tip deflection components are then transformed into the global coordinates (X_i, Y_i) using the coordinate transformation shown in equations (24a-b).

$$X_i = X_{t_i} + X_{i-1} \tag{24a}$$

$$Y_i = Y_{t_i} + Y_{i-1} \tag{24b}$$

where

$$\begin{bmatrix} cos\theta_{i-1} & -sin\theta_{i-1} \\ sin\theta_{i-1} & cos\theta_{i-1} \end{bmatrix} \begin{Bmatrix} X_{t_i} \\ Y_{t_i} \end{Bmatrix} = \begin{Bmatrix} l_i - \delta_{xlocali} \\ \delta_{ylocali} \end{Bmatrix}$$

The method for calculating the nodal deflections can be summarized as follows: the elastic moduli of the coating layer and copper foil, the geometry of the actuator, number of segments, and segment thicknesses are specified. The equivalent bending stiffness EI_e is then calculated. The system of equations in (15a-b) is solved for the curvature κ_i in equation (16a), the equivalent moment M_{eqi} from equation (17), and the local rotation angle θ_{0i} using equation (19). The local deflections $\delta_{xlocali}$ and $\delta_{ylocali}$ are then calculated using equations (21-22) and input into equations (23-24) to find the global segment-wise deflections X_i and Y_i.

3.6 Blocked Force

The force required to prevent deflection due to actuation, the blocked force, can be calculated for the end of any segment by simulating a cantilever beam with a constrained tip with an equivalent end-moment due to the actuation strain caused by Li insertion. This statically indeterminate beam can be solved using Castigliano's theorem. The strain energy due to bending is expressed as U, where $M(x)$ is the internal bending moment and F_{bi} is the blocked force required to prevent deflection at the end of segment i. Castigliano's theorem states the variation of the strain energy with respect to the blocked force is equal to the deflection at the tip, which for a propped beam is zero, as shown in equation (25). Equation (26) shows the calculated blocked force for a given equivalent end moment where the length of the beam is L.

$$\frac{\partial U}{\partial F_{bi}} = \int_0^L \frac{M}{EI_e} \frac{\partial M}{\partial F_{bi}} dx$$
$$= \frac{1}{EI_e} \int_0^L \left[M_{eq} + F_{bi}(x - L)\right](x - L) dx = 0 \tag{25}$$

$$F_{bi} = \frac{3M_{eq}}{2L} \tag{26}$$

4. RESULTS AND DISCUSSION

Experiments were conducted to measure the tip displacement of a unimorph of uniform thickness as a function of state of charge. The experimental setup and protocol are summarized briefly here and shown in Figure 3. [23]

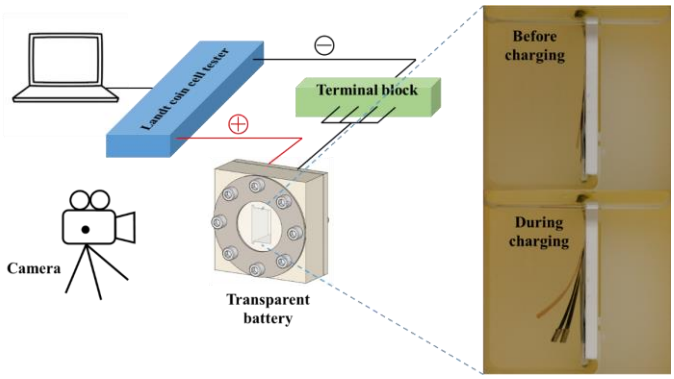

FIGURE 3: Transparent Battery Setup

To visualize the actuation process, a transparent battery was designed, fabricated and tested. The battery has a test chamber filled with electrolyte for anode deflection. A substrate is attached to the test chamber side wall, providing a base for the NCM cathode. Four unimorph Si anode cantilevers are paired with the cathode. Their bases are fixed at the substrate and the other ends are free to deform. Two of the anodes have a small Ni proof mass welded to their free end. During the test, the substrate is vertical to ensure the minimum effect of gravity on the anode shape. The battery is tested using a coin cell tester with constant current charge and discharge at C/20 rate (meaning a battery at 100% SOC can be fully discharged in 20 hours, with current being 0.26 mA). Figure 3 includes a view from a digital camera which captures anode motion. With image processing, the anode tip displacement data can be used to validate the unimorph actuator model.

The analytical model was used to predict the free deflection for a unimorph of uniform thickness and state of charge. Results are shown in Figure 4 along with the experimental data for a unimorph of width (w) 4mm, length (l) 30mm, coating thickness (h_{Ct}) of 6μm, copper foil thickness (h_{Cu}) of 34μm, coating elastic modulus (E_{Ct}) of 1GPa, and copper elastic modulus (E_{Cu}) of 120GPa.

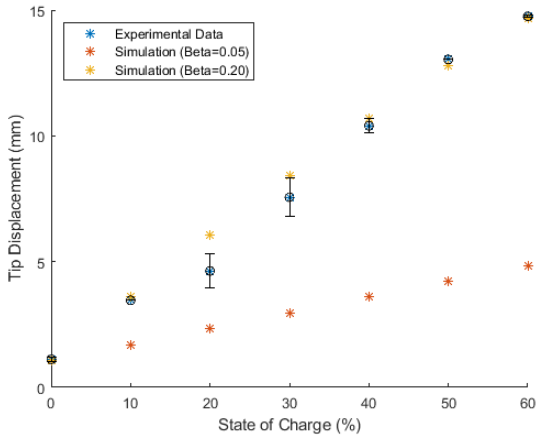

FIGURE 4. Tip displacement as a function of state of charge for uniform thickness and state of charge.

Figure 4 indicates that assuming a linear strain rate in the model of 5% is too low. This underestimate is attributed to the porous nature of the composite anode. As the Si nanoparticles expand they occupy voids left in the composite. The 5% linear strain rate estimated in previous work assumes complete occupation of the voids before the expansion begins to actuate the beam [22]. However, if the Si nanoparticle does not completely occupy the voids before actuating the entire beam, the linear strain rate will increase significantly. The results shown in Figure 4 imply that the expansion of the Si does not completely occupy the voids in the composite electrode. Instead, some of the expansion of these particles causes actuation strain rather than occupation of the voids that are still left. By increasing the linear strain rate to 20% in the model, the simulated tip displacement more closely matches the measured values, especially for higher states of charge. The small amount of initial curvature observed in the experiment at zero SOC is likely caused by electrode swelling during electrolyte immersion, and this initial curvature is accounted for in the simulated tip displacement.

Next, we consider the cases of uniformly varying and spatially varying state of charge. The model is used to simulate a single segment unimorph shown in Figure 5 and a five segment unimorph shown in Figure 6. Both of these unimorphs are modeled with a width (w) of 4mm, segment length (l) of 30mm, coating thickness (h_{Ct}) of 6μm, copper foil thickness (h_{Cu}) of 34 μm, coating elastic modulus (E_{Ct}) of 1GPa, copper elastic modulus (E_{Cu}) of 120GPa, and assumed linear strain rate β of 20%. Figure 5 shows a single segment at uniformly increasing SOC ranging from 0% SOC (blue) to 100% SOC (red) in increments of 25%.

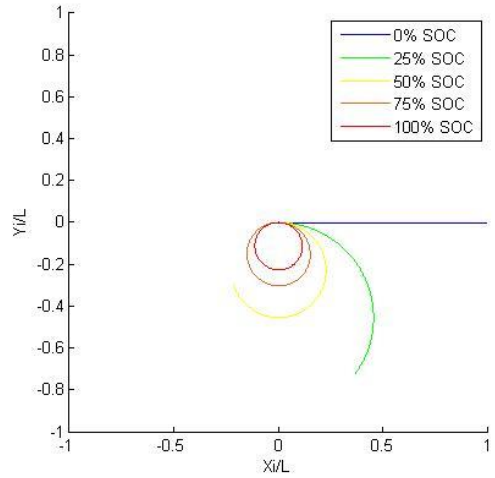

FIGURE 5. Predicted deflection along the length for single segment uniform SOC.

Figure 6 shows predicted deflection along the length of the beam for spatially varying SOC. The colored segmented beam shown in Figure 6 can be described as follows: Segment one closest to the root has a 0% SOC, segment

two has a 25% SOC (of 0.9680), segment three has a 50% SOC, segment four has a 75% SOC, and segment five at the tip is fully charged at 100% SOC (0.9680). Each segment maintains the same additional parameters as the previous figures with segment lengths of 30mm. Each beam pictured in gray represents spatially varying SOC with differing maximum states of charge. The beam with the lowest deflection has a 25% maximum SOC in beam five with each beam in between varying uniformly in SOC between 0% SOC and 25% SOC. The remaining gray beams follow the same format with a maximum SOC of 50% and 75%.

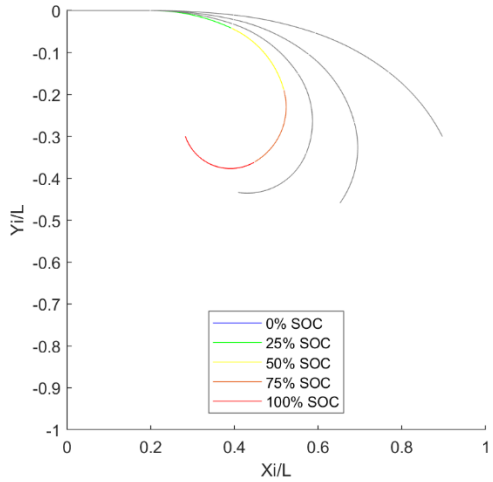

FIGURE 6. Predicted deflection along the length for spatially varying SOC.

Notice that the model is able to predict very large deflections, nonuniform curvature, and curling of the unimorph. Using the spatially varying SOC approach, it is thus possible for individually controlled and electrically isolated segments to achieve a complex actuated shape by varying the state of charge of each segment individually.

The model was then used to predict the displacement along the length of the beam for spatially varying thicknesses at constant state of charge (Figure 7). This five-segment unimorph has a length of (l) 30mm, width (w) of 4mm, coating thickness (h_{Ct}) of 6μm, coating elastic modulus (E_{Ct}) of 1GPa, copper elastic modulus (E_{Cu}) of 120GPa, assumed linear strain rate β of 20%, and 50% constant SOC. Segments one through five have respective copper foil thicknesses (h_{Ct}) of: 34, 30, 24, 18, and 12μm.

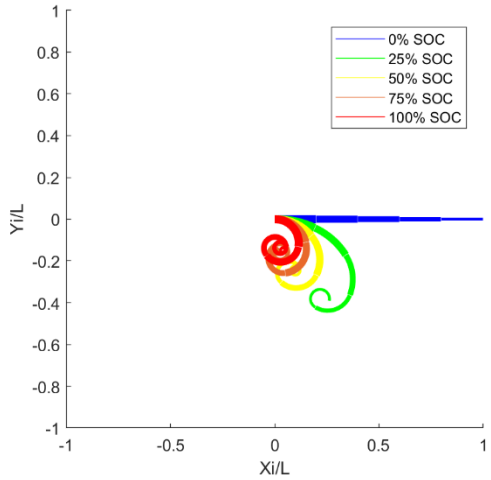

FIGURE 7. Predicted deflection along the length for spatially varying thicknesses at constant state of charge.

Figure 7 shows how the predicted deflection varies along the length of the beam with decreasing thickness at a constant state of charge. This configuration represents the electrically connected multi-segment beam configuration with a uniformly controlled state of charge. It can be observed that nonuniform curvature is achievable in this case, which would require less complex wiring and controllers than the previous case.

Finally, the blocked force case is considered in Figure 8. The model is used to predict the blocked force at the tip for a single segment unimorph with a length (l) of 30mm, width (w) of 4mm, coating thickness (h_{Ct}) of 6μm, copper foil thickness (h_{Cu}) of 34μm, coating elastic modulus (E_{Ct}) of 1GPa, copper elastic modulus (E_{Cu}) of 120GPa, assumed linear strain rate (β) of 20%, and uniformly increasing SOC.

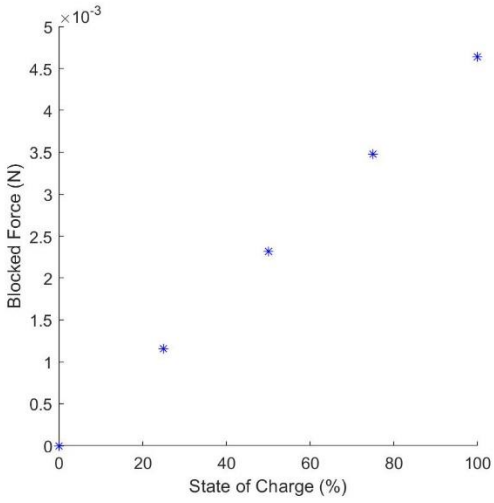

Figure 8. Blocked Force for Uniformly Varying State of Charge

It can be seen that the blocked force increases linearly with increasing SOC as would be expected. For the conditions specified, the maximum blocked at full charge is over 4.5mN for a beam 30mm long.

5. SUMMARY AND CONCLUSIONS

It has been shown that segmented unimorph actuators have the ability to form tailorable complex shapes depending on their geometry and state of charge. Depending on the application the geometry can be tailored to a specific formation. Increasing the coating thickness allows for greater deflection while increasing the copper foil thickness allows for decreased deflection. The blocked force can be increased by increased state of charge and coating thickness. The conditions given can be tuned to optimize for free deflection, blocked force, or a combination of deflection and actuation force.

Future work includes the extension of the model to include a second coating layer in a bimorph model. Further future modeling improvements include incorporation of the calculation of blocked force for segmented beams with spatially varying SOC and geometry. Experimental verification of deflection prediction along the length of the beam will also be conducted. The ability to tune the segmented actuator can be further expanded upon by including tailorable electrode designs. Tailored electrodes can allow the beam to form more complex shapes and achieve greater free deflection. Potential applications following further development include self-sensing, self-actuating, and self-powered active aids to rehabilitation as well as improving the performance of the next generation of soft robots.

ACKNOWLEDGMENTS

The authors gratefully acknowledge the support of the National Science Foundation under Grant No. 1662055.

REFERENCES

[1] Tarascon, J. M., and Armand, M., 2001, “Issues and Challenges Facing Rechargeable Lithium Batteries,” Nature, **414**(6861), pp. 359–367.

[2] Rahn, C. D.; Wang, C. Y., 2013, *Battery Systems Engineering*, John Wiley & Sons.

[3] Doyle, M., Fuller, T. F., and Newman, J., 1993, “Modeling of Galvanostatic Charge and Discharge of the Lithium/Polymer/Insertion Cell,” J. Electrochem. Soc., **140**(6), p. 1526.

[4] Wang, C. Y., Gu, W. B., and Liaw, B. Y., 1998, “Micro-Macroscopic Coupled Modeling of Batteries and Fuel Cells,” J. Electrochem. Soc., **145**(10), p. 3407.

[5] Fuller, T. F., Doyle, M., and Newman, J., 1994, “Simulation and Optimization of the Dual Lithium Ion Insertion Cell,” J. Electrochem. Soc., **141**(1), p. 1.

[6] Haran, B. S., Popov, B. N., and White, R. E., 1998, “Determination of the Hydrogen Diffusion Coefficient in Metal Hydrides by Impedance Spectroscopy,” J. Power Sources, **75**(1), pp. 56–63.

[7] Ning, G., and Popov, B. N., 2004, “Cycle Life Modeling of Lithium-Ion Batteries,” J. Electrochem. Soc., **151**(10), p. A1584.

[8] Santhanagopalan, S., Guo, Q., Ramadass, P., and White, R. E., 2006, “Review of Models for Predicting the Cycling Performance of Lithium Ion Batteries,” J. Power Sources, **156**(2), pp. 620–628.

[9] Tanim, T. R., Rahn, C. D., and Wang, C.-Y., 2014, “A Temperature Dependent, Single Particle, Lithium Ion Cell Model Including Electrolyte Diffusion,” J. Dyn. Syst. Meas. Control, **137**(1), p. 011005.

[10] Frecker, M. I., and Aguilera, W. M., 2004, “Analytical Modeling of a Segmented Unimorph Actuator Using Electrostrictive P(VDF-TrFE) Copolymer,” Smart Mater. Struct., **13**(1), pp. 82–91.

[11] Lallart, M., Richard, C., Sukwisut, P., Petit, L., Guyomar, D., and Muensit, N., 2012, “Electrostrictive Bending Actuators: Modeling and Experimental Investigation,” Sensors Actuators, A Phys., **179**, pp. 169–177.

[12] Crawley, E. F., and Anderson, E. H., 1990, “Detailed Models of Piezoceramic Actuation of Beams,” J. Intell. Mater. Syst. Struct., **1**(1), pp. 4–25.

[13] Low, T. S., and Guo, W., 1995, “Modeling of a Three-Layer Piezoelectric Bimorph Beam with Hysteresis,” J. Microelectromechanical Syst., **4**(4), pp. 230–237.

[14] Massad, J. E., Washington, G. N., and Sumali, H., 2005, “Orthotropic Deflection Model for Corner-Supported Plates with Segmented in-Plane Actuators,” R.C. Smith, ed., International Society for Optics and Photonics, p. 503.

[15] Massad, J. E., Sumali, H., Chaplya, P. M., and Martin, J. W., 2004, “Deflection Model for Corner-Supported Plates with Segmented in-Plane Actuators,” R.C. Smith, ed., International Society for Optics and Photonics, p. 309.

[16] Robbins, D. H., and Reddy, J. N., 1991, “Analysis of Piezoelectrically Actuated Beams Using a Layer-Wise Displacement Theory,” Comput. Struct., **41**(2), pp. 265–279.

[17] Vel, S. S., and Batra, R. C., 2001, “Analysis of Piezoelectric Bimorphs and Plates with Segmented Actuators,” Thin-Walled Struct., **39**(1), pp. 23–44.

[18] Kashyap, R., Lenka, T. R., and Baishya, S., 2015, “A Model for Doubly Clamped Piezoelectric Energy Harvesters With Segmented Electrodes,” IEEE Electron Device Lett., **36**(12), pp. 1369–1372.

[19] Cappelleri, D. J., Frecker, M. I., Simpson, T. W., and Snyder, A., 2002, “Design of a PZT Bimorph

Actuator Using a Metamodel-Based Approach," J. Mech. Des., **124**(2), p. 354.
[20] Shin, B. H., Choi, S.-W., Bang, Y.-B., and Lee, S.-Y., 2011, "An Earthworm-like Actuator Using Segmented Solenoids," Smart Mater. Struct., **20**(10), p. 105020.
[21] Howell, L. L., 2001, *Compliant Mechanisms*, Wiley.
[22] Ma, J., Rahn, C., and Frecker, M., 2017, "Multifunctional NMC-Si Batteries With Self-Actuation and Self-Sensing," ASME 2017 Conference on Smart Materials, Adaptive Structures and Intelligent Systems, Snowbird, Utah, USA.
[23] Ma, J., Gonzalez, C., Rahn, C., Frecker, M., and Wang, D., 2018, "Experimental Study of Multifunctional NCM-Si Batteries with Self-Actuation," ASME 2018 Conference on Smart Materials, Adaptive Structures and Intelligent Systems, San Antonio, Texas, USA.